

Ion-induced pattern formation on Co surfaces: An x-ray scattering and kinetic Monte Carlo study

O. Malis* and J. D. Brock

Cornell Center for Materials Research and School of Applied and Engineering Physics, Cornell University, Ithaca, New York 14853

R. L. Headrick†

Cornell High Energy Synchrotron Source, Cornell University, Ithaca, New York 14853

Min-Su Yi

Department of Materials Science and Engineering, Kwang-Ju Institute of Science and Technology, Korea

J. M. Pomeroy

Cornell Center for Materials Research and Department of Physics, Cornell University, Ithaca, New York 14853

(Received 26 January 2002; published 17 July 2002)

We report time-resolved grazing incidence small-angle x-ray scattering and atomic force microscope studies of the evolution of the surface morphology of the Co(0001) surface during low-energy Ar⁺ ion sputtering. At temperatures greater than 573 K, the surface is smooth, erosion proceeding in either a layer-by-layer mode or a step retraction mode. In contrast, at temperatures below 573 K, the surface develops a correlated pattern of mounds and/or pits with a characteristic length scale, λ . At room temperature, the surface morphology is dominated by mounds, and coarsens as time progresses. The characteristic length scale obeys the apparent power law, $\lambda = A \times t^n$ with $n = 0.20 \pm 0.02$. The rms roughness of the surface increases in time according to a similar power law with a slightly larger exponent $\beta = 0.28 \pm 0.02$. Kinetic Monte Carlo simulations of a simple model of Cu(111) were also performed. These simulations suggest that mound formation and coarsening at low temperatures is due to the slow diffusion of sputter-created adatoms on step edges. The morphological transition from mounds to pits is associated with activation of kink diffusion. These simple simulations produce values for the scaling exponents that agree with the experimental measurements.

DOI: 10.1103/PhysRevB.66.035408

PACS number(s): 68.55.-a, 61.10.-i, 81.05.Bx, 81.15.Jj

I. INTRODUCTION

Low-energy ion sputtering is widely used in semiconductor processing both to clean and pattern surfaces and as a component of analytical characterization techniques. Recent experiments demonstrated the potential of using ion etching to pattern surfaces on length scales smaller than those accessible via conventional photolithographic methods.¹ Two-dimensional arrays of metallic and semiconductor clusters with narrow size distributions and, at least, local positional order have been synthesized using ion erosion.¹⁻⁸ The exact morphology of these self-assembled patterns has been studied in detail only in a few material systems. It is known, however, that the surface morphology depends strongly on both the material structure and the temperature, as well as on the ion energy and the angle of incidence. Significant experimental and theoretical work remains before a level of control over self-assembled patterning that is sufficient for technological applications will be attained. This paper augments the currently available experimental information by studying the surface morphology induced by low-energy Ar⁺ ion irradiation of both single-crystal and polycrystalline surfaces of Co. Cobalt was chosen for these studies due to the technological importance of high-density magnetic storage devices. The combination of *in situ* x-ray scattering and reflectivity with *ex situ* atomic force microscopy (AFM) that we use is nearly ideal for time-resolved structural studies of the surface morphology, enabling detailed measurements of the effects of temperature, ion dose, and ion energy. Subsequent kinetic

Monte Carlo (KMC) simulations then provide insight into an atomic scale explanation of the behavior.

In spite of an extensive theoretical effort, our understanding of the microscopic mechanisms governing sputter erosion remains incomplete. The first successful model of ion erosion was proposed by Bradley and Harper (BH) to explain ripple formation on amorphous materials.⁹ The BH model relies on Sigmund's concept of a sputter rate that depends on the local curvature of the surface.¹⁰ In the BH model, a smooth surface is unstable to off-axis sputtering and develops a pattern of ripples with a characteristic wavelength and an exponentially diverging amplitude. Recent experimental^{11,12} and theoretical¹³ work extended the original BH model. These models successfully described a behavior exhibited by amorphous oxide and crystalline semiconductor surfaces during sputter erosion. However, they did not agree well with experimental observations on metallic surfaces. In particular, they did not explain the rich variety of morphologies observed on single-crystal noble-metal surfaces²⁻⁶ and several compound semiconductor surfaces.^{1,7,8} The most notable morphological characteristic of sputter erosion is coarsening, the increase in the size of surface features with ion dose. Coarsening cannot be produced by BH-type models, and has usually been explained by an analogy to coarsening during epitaxial growth. It is widely believed to be generated by instabilities arising from the kinetics of transient surface species such as adatoms or vacancies.

This paper first focuses on x-ray and AFM studies of the morphology induced by low-energy Ar⁺ ion sputtering on

single crystal and polycrystalline Co(0001) surfaces. The experimental setup used to make the x-ray scattering measurements is presented briefly in Sec. II. Above 573 K, erosion occurs in a two-dimensional or layer-by-layer mode and the surface remains relatively smooth. Section III focuses on the characterization of this high temperature regime and explains the method used to produce the starting surfaces for all subsequent experiments. Below 573 K, the Co surface roughens continuously and develops a pattern of characteristic features. Section IV describes in detail the morphology and time evolution of these features. To explore the microscopic processes involved in sputter etching, we performed KMC simulations of ion erosion. Section V presents the details of the simulations and the main results. The most significant diffusion processes and their role in determining the surface morphology in different temperature regimes are discussed in Sec. VI. Finally, we discuss the results of our investigation in Sec. VII and draw conclusions in Sec. VIII.

II. EXPERIMENTAL DETAILS

These experiments were performed in the A2 experimental station at the Cornell High Energy Synchrotron Source (CHESS) using a custom ultrahigh-vacuum thin-film growth/x-ray scattering chamber (base pressure 1.5×10^{-10} Torr). The thin-film growth/x-ray-diffraction chamber is a z -axis type of diffractometer and is described in detail elsewhere.¹⁴ The high x-ray flux (8×10^{13} photons/sec) available on the A2 experimental station at CHESS enabled us to perform x-ray-scattering measurements both *in situ* and in real-time. A set of sagittally-bent C/W multilayer crystals was used to select the x-ray energy of 12 keV and to horizontally focus the x-ray beam at the sample position.¹⁵ The samples were Co(0001) single crystals and polycrystalline Co films deposited by rf sputtering onto sapphire substrates. For the ion erosion experiments, the samples were sputtered at normal incidence with Ar^+ ions produced by a high flux Ion Tech (Veeco) rf source (4×10^{14} ions/cm²/sec at the sample). The ion energy of the Ion Tech source is adjustable between 100 and 700 eV. Prior to the experiment, the Co single crystals (miscut less than 0.25°) were cleaned by repeated cycles of annealing and sputtering at 643 K until surface contaminants were below the Auger detection limit.

Time-resolved specular x-ray reflectivity provides quantitative information about the evolution of the surface roughness during sputtering.¹⁶ Grazing-incidence small-angle x-ray scattering (GISAXS) is sensitive to correlations between surface features. The GISAXS was measured either with a point scintillation detector or with a 1024×1024 CCD detector produced by Medoptics (Dalsa Life Sciences, Tucson, AZ). In order to collect a scan with the point detector, the sputtering must be suspended, which results in a pulsed irradiation cycle. The CCD detector allows us to measure x-ray-scattering patterns without interrupting the sputtering process with an exposure time of half a second. Continuous sputtering, however, produced a rapid increase of the sample temperature with consequences that will be discussed below. Additional information about the final surface morphology was obtained *ex situ* using AFM.

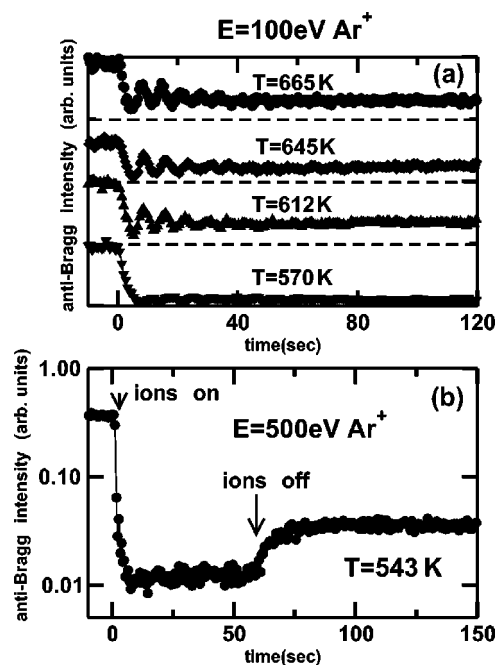


FIG. 1. (a) Time evolution of the specular anti-Bragg intensity during sputtering of a Co(0001) single crystal with 100-eV Ar^+ ions at several high temperatures. The curves are offset vertically for clarity. The zero intensity of each data set is at the level of the corresponding dashed curve. (b) Relaxation of anti-Bragg intensity after sputtering with 500-eV Ar^+ at 543 K.

III. HIGH-TEMPERATURE ION-EROSION REGIME OF COBALT(0001)

Previous experimental studies of low energy ion erosion of the single crystal surfaces of Pt, Ag, and Au identified two major morphological regimes. Above a well-defined transition temperature, the surface remains relatively smooth and erosion occurs by either a layer-by-layer or a step retraction mode. Below this transition temperature, the surface roughens rapidly, exhibiting a surface morphology consisting of mounds and/or pits or ripples. Cobalt follows the same general trends as the other close-packed metals, exhibiting a gradual transition to layer-by-layer and step-flow modes above 573 K.¹⁷ This is illustrated in Fig. 1(a), which shows the evolution of the intensity of the specularly reflected x-ray beam at the anti-Bragg condition during sputtering with 100-eV Ar^+ ions. The anti-Bragg condition in x-ray scattering is conceptually similar to the anti-phase condition in reflection-high-energy or low-energy electron diffraction. X-ray plane waves reflected from consecutive atomic layers are π out of phase, and the resulting intensity is maximally sensitive to single height steps on lateral length scales less than the x-ray coherence length. A large anti-Bragg intensity indicates a smooth surface, while a low anti-Bragg intensity indicates a rough surface. Above approximately 573 K, the anti-Bragg intensity exhibits oscillations indicative of a two-dimensional layer-by-layer erosion mechanism. To avoid the martensitic phase transformation to the cubic phase which could damage the crystal, the sample temperature was kept below 693 K at all times. Even under these conditions, it is clear that on the higher end of the available temperature

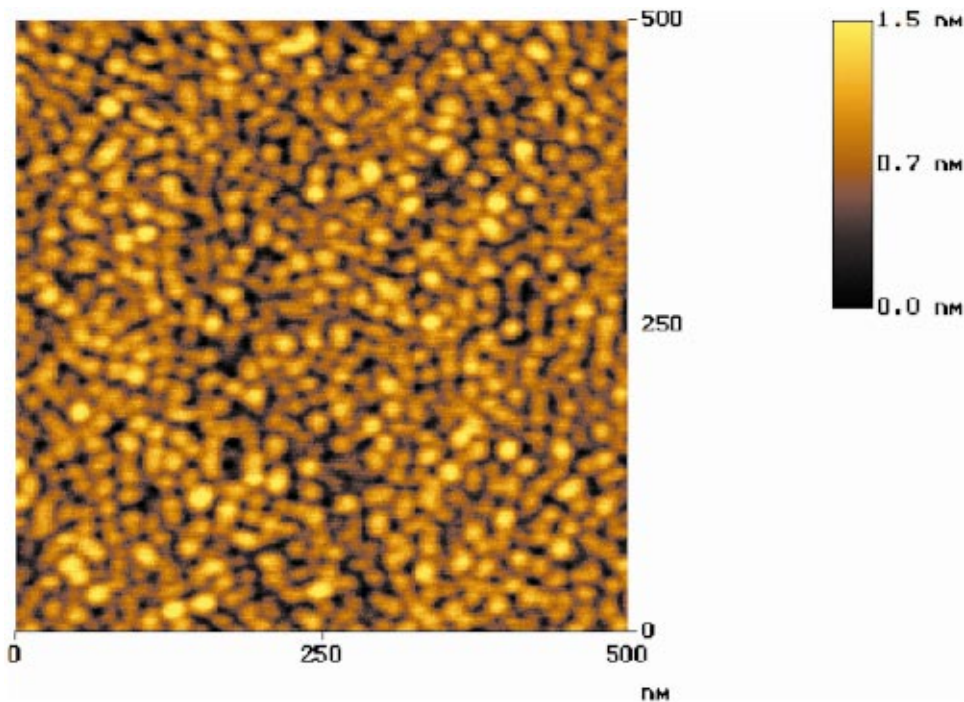


FIG. 2. (color) AFM image of a mounded surface pattern obtained by sputtering of a single-crystal Co(0001) surface with 500 eV Ar^+ ions for 60 seconds at room temperature.

range, the intensity oscillations dampen rapidly, indicating increasing roughness. Nevertheless, the intensity settles to a relatively high level, suggesting a smooth surface. The dependence of the final surface roughness on the energy of the incident ions has been discussed elsewhere.¹⁷

The smoothest surfaces (a rms roughness of ~ 1 Å) were obtained by sputtering with 500-eV Ar^+ ions at 643 K. Sputtering under these conditions rapidly and reliably produces flat surfaces even after extensive ion erosion at low temperatures. This ability to produce flat Co(0001) surfaces on demand was the crucial technical development that enabled the rest of this study. The smooth surfaces prepared using this recipe were utilized as the starting surfaces for all of the erosion measurements reported in this paper. We emphasize that neither heating nor sputtering alone results in a smooth surface.

As shown in Fig. 1(b), for ion energies greater than 200 eV, the anti-Bragg intensity increases after the irradiation is interrupted. This increase suggests that the surface continues to smoothen due to the redistribution of mobile species. At these relatively high temperatures, the diffusion of adatoms is effectively instantaneous on the time-scale of the experiment, a fact confirmed by our studies of homoepitaxial Co growth. The vacancies produced in the sputtering process, however, are considerably slower than the adatoms as they need to overcome higher diffusion activation barriers. If we assume that the average terrace width is $x = 1000$ Å, we can use the relaxation time of the x-ray intensity τ to estimate the diffusion constant $D = x^2 / \pi^2 a^2 \tau$, where a is the lattice constant.¹⁸ If the diffusion constant has an Arrhenius dependence on the activation energy, $D = \nu_0 \exp(-E_v / k_B T)$, where $\nu_0 = 10^{12} \text{ s}^{-1}$, we estimate the vacancy diffusion barrier E_v to be approximately 0.97 eV. This value is relatively large but is consistent with theoretical calculations of the activation energy for vacancy diffusion on Cu(111) (0.618 eV).¹⁹

We will discuss the effects of vacancy diffusion in more detail in Sec. VI.

IV. LOW-TEMPERATURE PATTERN FORMATION ON COBALT SURFACES

Below 573 K the Ar^+ ion bombardment of single crystal Co(0001) rapidly roughens the surface and gives rise to a pattern of mounds or pits. This regime may be further separated into temperature ranges that produce qualitatively different morphologies. We know from recent experimental work that between 473 and 573 K the surface morphology is dominated by pits, while from room temperature up to 473 K the surface exhibits a mostly mounded pattern.¹⁷ As an example, Fig. 2 shows a typical AFM image of the mounded structure produced at room temperature by irradiation with 500-eV Ar^+ ions for 60 sec. In order to characterize in detail the evolution of the surface morphology, we measured *in situ* and in real time the grazing incidence small angle x-ray scattering. Figure 3(a) shows a 512×512 pixel CCD image of the GISAXS intensity in the vicinity of the specular rod corresponding to the mounded surface pattern displayed in Fig. 2. The evolution of this x-ray pattern as a function of time is schematically shown in Fig. 3(b). Each of the curves in Fig. 3(b) represents a cross-section of the CCD image in the vertical direction which corresponds to a direction parallel to the surface in reciprocal space, q_{\parallel} . Shortly after starting the ion bombardment, the GISAXS pattern develops a set of growing satellite peaks which indicate that the surface exhibits a pattern of correlated mounds or pits with a characteristic wavelength. With increasing ion dose the peaks shift in, indicating that the features coarsen similar to the behavior observed in other metal systems.²⁰

Figure 4 shows the evolution of the average mound/pit separation calculated from the inverse of the peak splitting

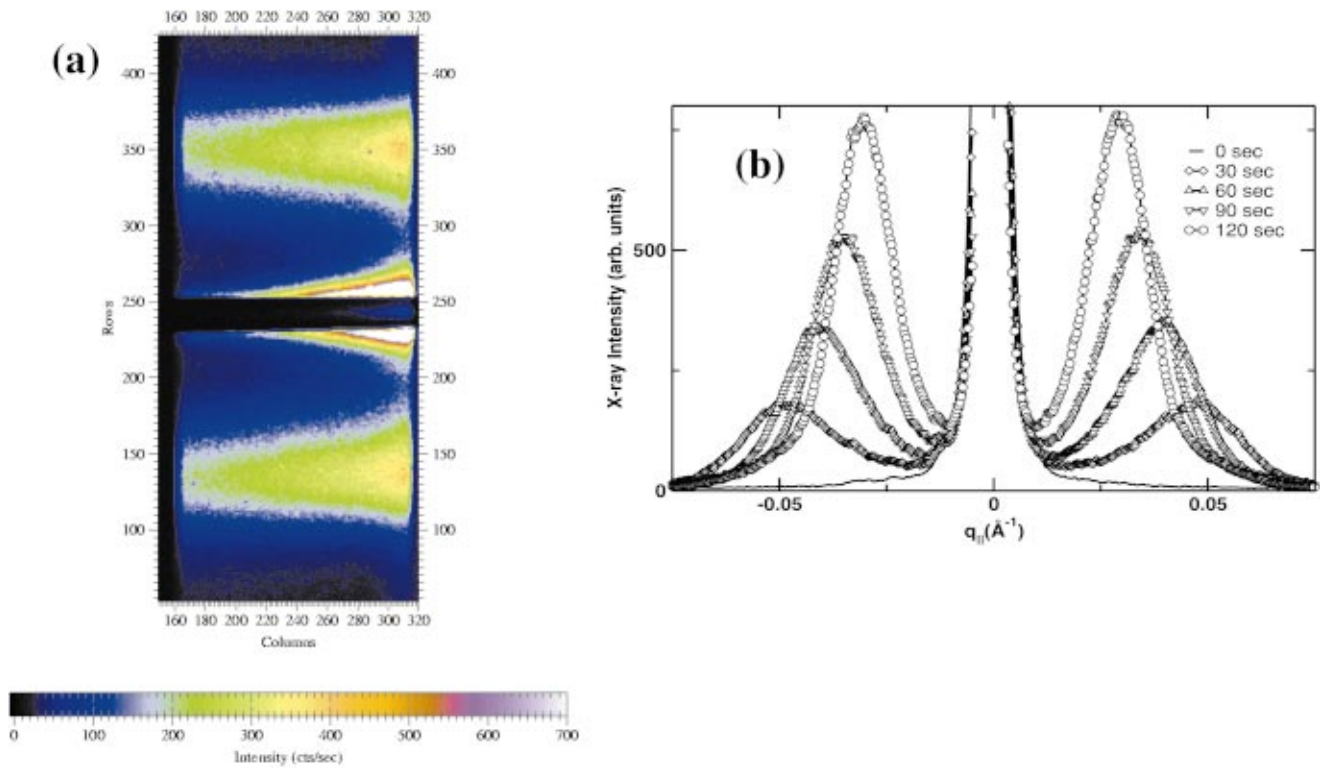


FIG. 3. (color) (a) CCD image of GISAXS intensity corresponding to the mounded Co(0001) single-crystal surface shown in Fig. 2 (60-sec irradiation with 500-eV Ar^+ ions at room temperature). The specular region of the intensity was blocked with a beam stop (black horizontal line in the center of the image) to avoid blooming into the neighboring pixels. (b) Evolution of the GISAXS intensity during sputtering with 500-eV Ar^+ ions of a Co(0001) single-crystal surface. Each curve represents a vertical cross section of a CCD image like the one shown in (a), and corresponds to a scan of the specular rod in the direction parallel to the sample surface.

for several incident ion energies at room temperature. For low energy and ion fluxes the mound separation, λ , follows a power law in time, $\lambda = At^n$, with an exponent n between 0.17 and 0.22. For high Ar^+ fluxes or energies, the ion bombardment causes a significant heating of the sample. This effect is particularly strong for continuous irradiation at energies above 200 eV. For example in the case of continuous irradiation

with 500-eV ions shown in Fig. 3, the total drift in temperature from beginning to end of scan is 115 K. If we assume that the entire ion energy contributes to sample heating and there are no radiative or conductive heat losses to the sample holder, then we can estimate the heating rate due to ion irradiation to approximately 7 K/min. This value accounts for only half of the observed heating effect and suggests that there is also a significant contribution due to the infrared radiation from the hot ion source.

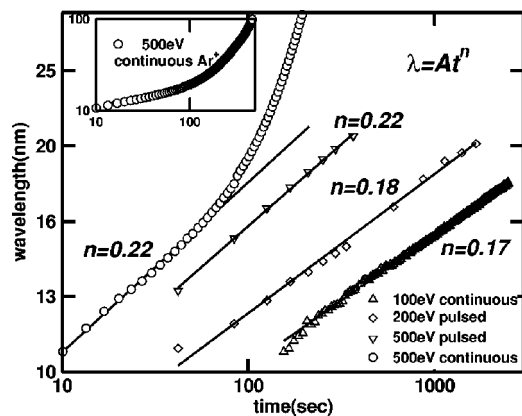


FIG. 4. Time evolution of the average mound separation during Ar^+ irradiation with 100-, 200- and 500-eV ion energies of a Co(0001) single crystal surface at room temperature. For the pulsed irradiation experiments, the time refers to the accumulated sputtering time.

As the temperature drifts up, the surface diffusivity increases and causes an additional coarsening of the mounds which is reflected in the unusually fast increase of the feature separation length (inset of Fig. 4). The heating problem is not so severe for a low ion energy (only 20 K for the 100-eV Ar^+ erosion) and for pulsed irradiation measurements. Therefore we believe that the exponent extracted from the pulsed irradiation data at 500 eV, $n = 0.22$, is accurate for this ion energy. This value is also consistent with the fit of the early time data in the case of continuous irradiation.

The evolution of the rms roughness σ can also be followed by measuring the specular intensity. If we assume that the roughness is small ($\sigma q < 1$), the x-ray intensity is proportional to $\exp(-\sigma^2 q^2)$, where q is the component of the momentum transfer perpendicular to the surface defined by $q = 4\pi/\lambda \sin \theta$. λ is the x-ray wavelength and $\theta = 0.75^\circ$ is half the angle between the incident and scattered radiation. Figure 5 displays the time evolution of the extracted roughness

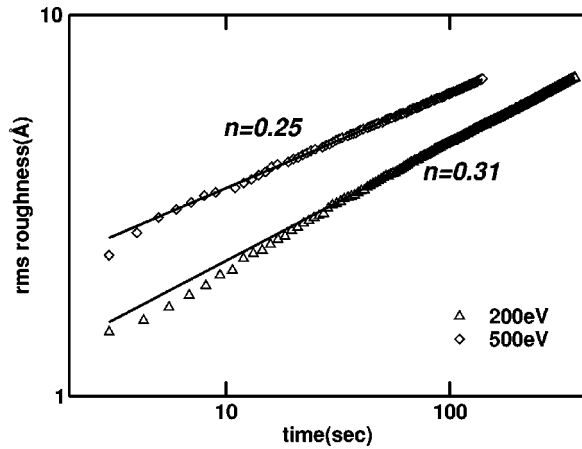


FIG. 5. Time evolution of the rms roughness during irradiation of Co(0001) single crystal with 200- and 500-eV Ar^+ ions, respectively, at room temperature.

ness during continuous irradiation with 200- and 500-eV Ar^+ ions of a Co(0001) surface. The roughness can be fit with a power law in time with an average exponent $\beta = 0.28 \pm 0.03$.

In order to explore the potential of using ion etching to produce arrays of nanoscale features for technological applications, we have also studied the effect of low-energy ion sputtering on the surfaces of polycrystalline Co films. We deposited 1000-Å-thick Co films on C-axis sapphire at different temperatures and studied the morphology induced by Ar^+ ion irradiation at room temperature. Only high-quality epitaxial films (in-plane rocking curve width less than 1.5°) with grain sizes of the order of 3000 Å, grown at 623 K exhibited a pattern formation similar to the single crystal Co. At room temperature the mounds also grow with increasing ion dose but the coarsening exponent is significantly lower than for the single crystal ($n=0.09$). This low value suggests that coarsening is influenced by extrinsic effects, such as the grain size.

V. KINETIC MONTE CARLO SIMULATIONS OF COPPER(111)

In order to gain insight into the microscopic processes involved in low-energy ion sputtering of closed packed metals, we performed kinetic Monte Carlo simulations of ion erosion. The (111) surface of copper rather than cobalt was simulated because we did not have access to all the necessary Co potentials at the time of this investigation. For Cu(111) we were able to utilize a realistic theoretical model, the effective-medium theory (EMT) of cohesion in metals,²¹ to generate the required potentials. EMT is known to give a good qualitative description of Cu and offers complete information about surface diffusion processes. We believe, however, that the results presented here are not element dependent. This notion is supported by preliminary simulations of ion erosion on Au(111). However, in order to directly compare temperatures between the cobalt and copper, it is necessary to scale the temperatures by the melting points of the two elements. For example, temperatures quoted in this sec-

tion may be multiplied by a factor of 1.3 to make comparisons to the temperatures quoted for cobalt in previous sections. We will describe below that after converting temperatures in this manner, we find a good agreement in the rough/smooth transition, as well as in the low temperature mound/pit transition.

The effect of the ion impact was modeled by randomly removing atoms from the (111) surface of a $200 \times 200 \times 200$ atom cubic cell. The program allows the removal of multiple atoms as well as the creation of adatom-vacancy pairs. However, to reproduce closely the experimental conditions we will focus on the case of single atom removal which corresponds to a sputtering yield of 1. This value is reasonable for Co sputtering with Ar^+ ions in the 100 to 500 eV energy range. The ion flux in the simulations was typically 9×10^{16} ions/cm² s. The KMC algorithm used to simulate the thermal diffusion has been presented in detail elsewhere.²² For every atom configuration at a certain temperature, all possible single atom diffusion processes are identified and added to a list of potential moves. The rate of each process is evaluated according to $r_i = \nu_0 \exp(-E_i/k_B T)$, where the common prefactor ν_0 is taken to be $\nu_0 = 10^{12} \text{ s}^{-1}$ for simplicity. The diffusion barriers E_i were estimated using the Artwork software package²³ which implements the EMT potentials for Cu and allows the energy calculation for an arbitrary surface configuration. The results for the adatom diffusion barriers on terraces and steps are identical with published values.¹⁹ Additional barriers were calculated for vacancy motion and annihilation with adatoms and step edges.

We find that above 500 K this model exhibits a layer-by-layer removal mechanism consistent (after temperature scaling) with the experimental observations presented in Sec. III for Co, and with other results reported in the literature.^{2,6} If the temperature is lowered below 460 K, the amplitude of the anti-Bragg oscillations decays continuously, indicating a transition to the patterning regime.

Figure 6(a) shows the surface morphology after removal of 20 ML at 232 K. This simulation may be compared to the room-temperature image for cobalt in Fig. 2. At this temperature the surface develops a morphology characterized by compact mounds with a narrow size distribution, in agreement with the experimental observations. The mounds are separated by inter-connected valleys with irregular shapes and rough contours. The average mound size was calculated from the first zero of the autocorrelation function. Figure 7 shows the time evolution of the mound size and rms roughness for erosion at 232 and 290 K, respectively. Both the mound size and the rms roughness follow the expected power-law time dependence. At 232 K the coarsening exponent $n=0.21$ agrees well with our experimental observations for Co(0001). The roughness exponent β takes a slightly larger value, $\beta=0.26$, also consistent with our measurements.

Above approximately 290 K, the simulations predict a qualitative change in the structure of the surface pattern induced by erosion. Figure 6(b) shows this high-temperature morphology corresponding to the removal of 20 atomic monolayers at 348 K. The image indicates the development

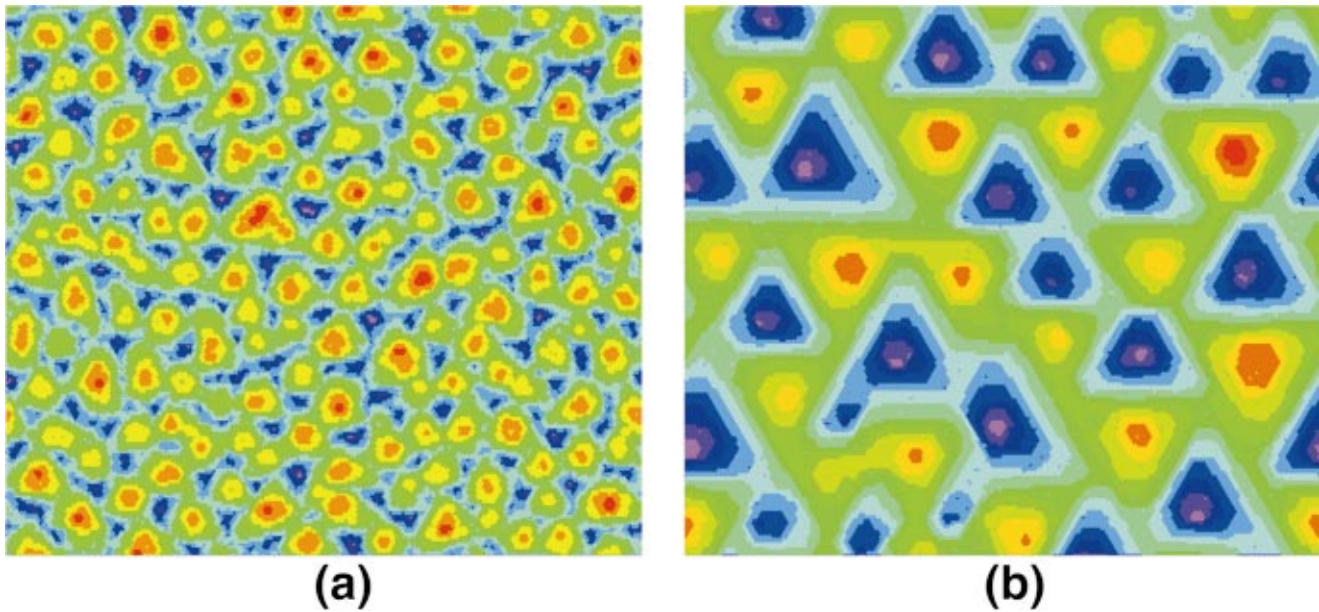


FIG. 6. (color) Simulated surface morphologies corresponding to the removal of 20 ML at 232 K (a), and 348 K (b), respectively. The morphology of the lower-temperature surface is dominated by compact mounds. In contrast, the morphology of the higher-temperature surface is dominated by large triangular pits. The size of the images is $51 \times 44 \text{ nm}^2$. The surface height is represented by a rainbow color scale from violet (lowest level) to red (highest level). The total height range is 2 nm.

of a pattern dominated mostly by large, triangular pits with smooth contours and uniform size. In this regime, the rms roughness and average feature size also follow a power law, but both exponents appear to take larger values and to increase with increasing temperature. At 290 K, for instance, the asymptotic coarsening exponent is $n=0.25$ while the roughness exponent is $\beta=0.3$ (Fig. 7).

VI. ATOMISTIC MECHANISMS

The KMC simulations provide detailed information about the diffusion processes active in different temperature

ranges. Figure 8 schematically shows the most important atomic moves occurring in the simulations. We will first discuss the low temperature case. At 232 K, the vacancies deposited on the surface do not participate directly in the mass transport. The vacancies deposited far from the edges [Fig. 8(a)] need to overcome large energy barriers (0.618 eV) in order to diffuse on the terrace and no motion is observed. Only the vacancies deposited within one lattice constant from downhill edges can attach to the edge creating a step advancement [Fig. 8(b)]. Furthermore, the activation energy for diffusion of step advancements along step edges is also large (0.44 eV) and therefore this process is suppressed at low

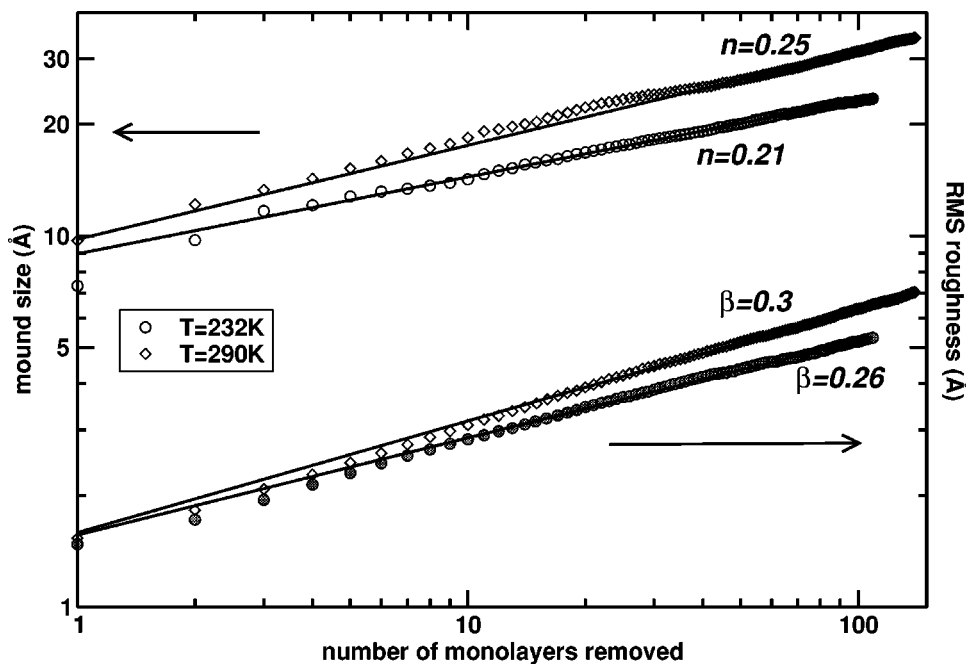


FIG. 7. Time evolution of the feature size (hollow symbols) and rms roughness (filled symbols) from the KMC simulations of sputtering at 232 K (circles) and 290 K (diamonds), respectively.

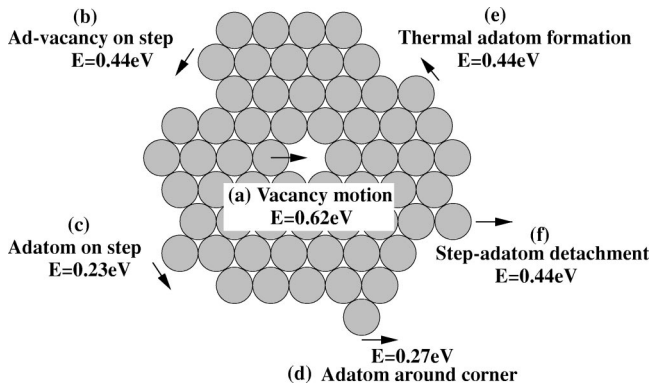


FIG. 8. Energy barriers for step-adatom, vacancy, and kink diffusion on the Cu(111) surface calculated using EMT.

temperatures. Consequently, mass transport on the surface is dominated by adatom diffusion, in particular by the diffusion of adatoms on step edges [Figs. 8(c) and 8(d)].

Step adatoms are the atoms attached to the islands by one or two bonds [Figs. 8(c) and 8(d)]. In our simulations there is no net deposition of atoms, but we also found that adatom-vacancy pair creation does not change the phenomenology discussed below. The barrier for thermal detachment of step adatoms from kinks is significant [Fig. 8(e)], and therefore, at 232 K, the step adatoms are created mainly by atom removal from edges, in particular from special edge configuration, such as kinks. Because the step adatoms are produced in the sputtering process, their concentration is very low. Moreover, due to the non-negligible diffusion activation energy (0.22 eV), the step adatoms have a very limited mobility along step edges. They can diffuse along steps only until they encounter kinks which trap them irreversibly. This process results in a slow edge diffusion current which promotes convex edge contours and compact islands. The islands stack up to build a mounded structure similar to the one observed in experiments.

If the simulation temperature is increased above 290 K, the vacancy diffusion becomes important and eventually dominates the mass transport on the surface. First the thermal atom detachment from kinks [Fig. 8(e)] and the ad-atom motion [Fig. 8(b)] begin to play a role in edge diffusion as can be seen from the statistics of the atomic moves. Both processes generate an effective line tension that smoothes the concave step edges surrounding surface depressions, and favors the formation of large, compact pits. Since both kink detachment and kink diffusion are thermally activated, the concentration of mobile species is considerably larger than in the low temperature case, and produces an effectively faster edge diffusion process. The edge diffusion is also enhanced by the formation of extended diffusion paths along causeways separating the pits that enable long-distance mass transport. While step adatoms were observed to significantly contribute to surface relaxation, adatom detachment from steps [Fig. 8(f)] occurred very infrequently. At even higher temperatures, it is expected that vacancies become mobile on the terraces and contribute additionally to the edge diffusion.

VII. DISCUSSION

The evolution of ion-induced surface patterning is generally understood by analogy with mound formation in homoepitaxial growth. During thermal deposition at low temperatures, atoms landing on terraces encounter a significant barrier for descent at downhill step edges, the Ehrlich-Schwoebel (ES) barrier, and attach primarily to uphill step edges. This diffusion asymmetry at step edges generates a net uphill current that destabilizes a smooth surface and leads to the formation and coarsening of mounds. Siegert and Plischke²⁴ examined the effect of the ES current, and proposed a model for mound coarsening that involves slope selection. For surfaces with triangular symmetry such as hexagonal (0001) or cubic (111), the mound size should increase in time according to a power law with an exponent equal to 0.33.²⁵ Recently several studies emphasized the importance of edge diffusion for pattern formation during growth.^{26,27} Murty and Cooper found that edge diffusion can lead to mound formation even in the absence of an Ehrlich-Schwoebel barrier.²⁶ Amar²⁷ also performed Monte Carlo simulations to investigate the role of corner diffusion during growth on surfaces with (100) and (111) symmetries. For (111) surfaces he found that slow edge diffusion around corners can lower the scaling exponent from the expected theoretical value of 0.33 to 0.22.

Low-energy ion sputtering is a significantly more complicated process than thermal deposition. In the first approximation the ion interaction with a crystalline material can be viewed as a deposition of surface vacancies. However, as pointed out recently by Costantini *et al.*,⁴ the phenomenology of ion erosion cannot be derived simply by inverting the growth process. If this were the case, sputtering would always produce a pit morphology as observed in experiments at high temperatures. For most materials, though, ion irradiation below room temperature produces a mounded pattern, very similar in fact to the pattern generated by thermal deposition. The origin of the morphological transition from mounds to pits is not very well understood at this point. Costantini *et al.*⁴ examined in detail defect formation during ion sputtering of Ag(001), and showed that, in addition to vacancy creation, ion bombardment results in the formation of complex defects, such as adatom and vacancy clusters. Busse *et al.*²⁸ also attributed the initial monolayer growth observed during ion bombardment of Al(111) to the formation of extensive subsurface vacancy defects and surface adatom clusters. Therefore, for high-energy ions and low melting point materials (Ag, Al) the approximation of sputtering as vacancy deposition may not be accurate. Even in the absence of complex defects, the difference between the mobility of the adatoms and vacancies on (111) and (0001) surfaces breaks the symmetry between deposition and erosion and, arguably, plays a role in determining the surface morphology.

To distinguish between the contributions of the ion collisions and the surface kinetics which follow the ion impact, we have performed kinetic Monte Carlo simulations of Cu(111), as discussed in Sec. V. Our simulations approximate the ion impact by depositing vacancies but accurately

describe the diffusion processes associated with both vacancies and adatoms. Using just surface diffusion and vacancy deposition, our model reproduces the most important characteristics of the ion-induced surface morphologies. In particular, it reproduces the morphological transition from a mounded pattern at lower temperatures to a pit-dominated structure at higher temperatures.²⁹ Regardless of the temperature, the surface features coarsen in time according to a power law. The inclusion of adatom-vacancy pairs and deposition of multiple vacancies per event did not change this phenomenology.

In the low temperature regime, where slow adatom step diffusion is dominant, our KMC simulations predict a relatively low value for the coarsening exponent ($n=0.21$). This value is consistent with the results of Monte Carlo simulations of growth with slow edge diffusion²⁷ and of other Monte Carlo simulations of sputtering.³ Above 290 K, the faster kink diffusion process causes the increase of n with temperature toward the theoretical prediction $n=0.33$. Michely *et al.*³ also emphasized the importance of thermal step-adatom detachment from kinks. They found that if this diffusion mechanism is completely suppressed, the scaling exponent decreases from $n=0.22$ to 0.09.

VIII. CONCLUSIONS

Using time-resolved x-ray scattering techniques, AFM, and KMC simulations we have studied the morphology induced by low-energy ion erosion on the surface of closed-packed metals. The experimental studies focus on Co, a metal of interest for technological applications. Ar⁺ ion erosion of single crystal Co(0001) above 573 K occurs in a two-dimensional or layer-by-layer mode. In this regime the ions have a smoothing effect and can be used to prepare atomically flat surfaces at relatively low temperatures ($T < 400$ °C). We have used the surface relaxation time following ion irradiation to estimate a diffusion activation barrier of vacancies on Co(0001) (0.97 eV) which is consistent with theoretical calculations for fcc metals.

Below 573 K, ion erosion produces a pattern of mounds a pits with a narrow size distribution. At room temperature, the mounds coarsen in time, the average mound separation following a power law with an exponent of $n=0.20 \pm 0.02$. The rms roughness also follows a power law in time with an average exponent $\beta=0.28$. These values are consistently lower than the results reported in the literature for Pt(111) ($n=0.28 \pm 0.02, \beta > 0.34$),³ Cu(110) ($n=0.26 \pm 0.02, \beta$

$= 0.43 \pm 0.08$),⁵ Au ($n=\beta=0.27 \pm 0.02$),⁶ and InP ($n=0.26 \pm 0.04, \beta=0.27 \pm 0.06$).⁷

In order to investigate the microscopic processes involved in ion sputtering of closed packed metals, we have performed KMC simulations of Cu(111) erosion. The simulations reproduce the most significant morphological transitions characteristic to ion etching. At approximately 460 K the simulations predict a transition from layer-by-layer removal at high temperatures, to pattern formation at low temperatures. In the roughening regime, the simulations also reproduce a morphological transition from mound formation below 290 K to pit formation above 290 K.

A detailed analysis of the diffusion processes active during erosion revealed that step edge diffusion of sputter-created step adatoms is the main cause of mound formation at the lowest temperatures. This mechanism is essentially identical to the step-edge diffusion active during epitaxial growth and explains the similarity of the resulting morphologies. In this regime the simulations predict scaling exponents ($n=0.21, \beta=0.28$) in agreement with our experimental results for Co. Above 290 K, kink dissociation and diffusion become active and eventually dominate the edge diffusion process, resulting in a morphological transition from mounds to pits. As a consequence of the faster edge diffusion, the coarsening exponent increases to $n=0.25$ and the roughening exponent increases to $\beta=0.3$. These larger values are consistent with the experimental reports for Pt, Ag, and Au, and agree with the general assumption that kink diffusion is the dominating diffusion mechanism at the respective temperatures. The lower values of the scaling exponents we observe for Co(0001) are most likely due to higher diffusion barriers,³⁰ which suppress kink mobility at room temperature. Our studies of pattern formation on epitaxial films also suggested that if the surface diffusion is additionally slowed down by the presence of defects such as grain boundaries the coarsening exponent decreases further to $n=0.09$.

ACKNOWLEDGMENTS

The authors benefited greatly from discussions with Jim Sethna, Marcus Rauscher, Jacob Jacobsen, and Aaron Couverture. This work was supported by the Cornell Center for Materials Research (CCMR), a Materials Research Science and Engineering Center of the National Science Foundation (DMR-0079992). This work is based upon research conducted in part at the Cornell High Energy Synchrotron Source (CHESS) which is supported by the National Science Foundation under Award No. DMR-9713424.

*Current address: IQE Incorporated, 119 Technology Drive, Bethlehem, Pennsylvania 18015

†Current Address: Department of Physics, Cook Physical Sciences Building, University of Vermont, Burlington, Vermont 05405-0125

¹S. Facsko, T. Dekorsy, C. Koerdt, C. Trappe, H. Kurz, A. Vogt, and H.L. Hartnagel, *Science* **285**, 1551 (1999).

²T. Michely, T. Land, U. Littmark, and G. Comsa, *Surf. Sci.* **272**, 204 (1992).

³T. Michely, M. Kalf, G. Comsa, M. Strobel, and K.H. Heinig, *Phys. Rev. Lett.* **86**, 2589 (2001).

⁴G. Costantini, E.B. de Mongeot, C. Boragno, and U. Valbusa, *Phys. Rev. Lett.* **86**, 838 (2001).

⁵S. Rusponi, G. Costantini, C. Boragno, and U. Valbusa, *Phys. Rev. Lett.* **81**, 2735 (1998).

⁶M.V.R. Murty, T. Curcic, A. Judy, B.H. Cooper, A.R. Woll, J.D. Brock, S. Kycia, and R.L. Headrick, *Phys. Rev. Lett.* **80**, 4713 (1998).

⁷F. Frost, A. Schindler, and F. Bigl, *Phys. Rev. Lett.* **85**, 4116 (2000).

⁸J. Erlebacher, M.J. Aziz, E. Chason, M.B. Sinclair, and J.A. Floro,

- Phys. Rev. Lett. **82**, 2330 (1999).
- ⁹R.M. Bradley and J.M.E. Harper, J. Vac. Sci. Technol. A **6**, 2390 (1988).
- ¹⁰P. Sigmund, J. Mater. Sci. **8**, 1545 (1973).
- ¹¹T.M. Mayer, E. Chason, and A.J. Howard, J. Appl. Phys. **76**, 1633 (1994).
- ¹²C.C. Umbach, R.L. Headrick, and K.C. Chang, Phys. Rev. Lett. **87**, 246104 (2001).
- ¹³R. Cuerno and A.L. Barabasi, Phys. Rev. Lett. **74**, 4746 (1995).
- ¹⁴R.L. Headrick, S. Kycia, Y.K. Park, A.R. Woll, and J.D. Brock, Phys. Rev. B **54**, 14686 (1996).
- ¹⁵R. Headrick, K. Smolenski, A. Kazimirov, C. Liu, and A. Macrander, Rev. Sci. Instrum. **73**, 1476 (2002).
- ¹⁶R. Feidenhansl, Surf. Sci. Rep. **10**, 105 (1989).
- ¹⁷O. Malis, J.M. Pomeroy, R.L. Headrick, and J.D. Brock, in *Ion Beam Synthesis and Processing of Advanced Materials*, edited by S.C. Moss, K.-H. Heinig, and D.B. Poker, MRS Symposia Proceedings No. **647** (Materials Research Society, Pittsburgh, 2000), p. O9.5.1.
- ¹⁸J.A. Venables, G.D.T. Spiller, and M. Hanbucken, Rep. Prog. Phys. **47**, 399 (1984).
- ¹⁹P. Stoltze, J. Phys.: Condens. Matter **6**, 9495 (1994).
- ²⁰M.V.R. Murty, A.J. Couture, B.H. Cooper, A.R. Woll, J.D. Brock, and R.L. Headrick, J. Appl. Phys. **88**, 597 (2000).
- ²¹K.W. Jacobsen, J.K. Norskov, and M.J. Puska, Phys. Rev. B **35**, 7423 (1987).
- ²²J. Jacobsen, B.H. Cooper, and J.P. Sethna, Phys. Rev. B **58**, 15847 (1998).
- ²³P. Stoltze, *Simulation Methods in Atomic-Scale Materials Physics* (Polyteknisk Forlag, Lyngby, Denmark, 1997).
- ²⁴M. Siegert and M. Plischke, Phys. Rev. Lett. **73**, 1517 (1994).
- ²⁵M. Siegert, Phys. Rev. Lett. **81**, 5481 (1998).
- ²⁶M.V.R. Murty and B.H. Cooper, Phys. Rev. Lett. **83**, 352 (1999).
- ²⁷J.G. Amar, Phys. Rev. B **60**, R11317 (1999).
- ²⁸C. Busse, H. Hansen, U. Linke, and T. Michely, Phys. Rev. Lett. **85**, 326 (2000).
- ²⁹A. J. Couture, Ph.D. thesis, Cornell University, 2000.
- ³⁰J.E. Prieto, J. de la Figuera, and R. Miranda, Phys. Rev. B **62**, 2126 (2000).